The Astrophysical Journal, 707:593–603, 2009 December 10 doi:10.1088/0004-637X/707/1/593

ENERGY SPECTRA OF COSMIC-RAY NUCLEI AT HIGH ENERGIES

H. S. Ahn[1], P. Allison[2], M. G. Bagliesi[3], L. Barbier[4], J. J. Beatty[2], G. Bigongiari[3], T. J. Brandt[2], J. T. Childers[5], N. B. Conklin[6], S. Coutu[6], M. A. DuVernois[5], O. Ganel[1], J. H. Han[1], J. A. Jeon[7], K. C. Kim[1], M. H. Lee[1], P. Maestro[3,11], A. Malinine[1], P. S. Marrocchesi[3], S. Minnick[8], S. I. Mognet[6], S. W. Nam[7], S. Nutter[9], I. H. Park[7], N. H. Park[7], E. S. Seo[1,10], R. Sina[1], P. Walpole[1], J. Wu[1], J. Yang[7], Y. S. Yoon[1,10], R. Zei[3], and S. Y. Zinn[1]

[1] Institute for Physical Science and Technology, University of Maryland, College Park, MD 20742, USA
[2] Department of Physics, Ohio State University, Columbus, OH 43210, USA
[3] Department of Physics, University of Siena and INFN, Via Roma 56, 53100 Siena, Italy
[4] Astroparticle Physics Laboratory, NASA Goddard Space Flight Center, Greenbelt, MD 20771, USA
[5] School of Physics and Astronomy, University of Minnesota, Minneapolis, MN 55455, USA
[6] Department of Physics, Penn State University, University Park, PA 16802, USA
[7] Department of Physics, Ewha Womans University, Seoul 120-750, Republic of Korea
[8] Department of Physics, Kent State University, Tuscarawas, New Philadelphia, OH 44663, USA
[9] Department of Physics and Geology, Northern Kentucky University, Highland Heights, KY 41099, USA
[10] Department of Physics, University of Maryland, College Park, MD 20742, USA
Received 2009 August 27; accepted 2009 October 22; published 2009 November 24

ABSTRACT

We present new measurements of the energy spectra of cosmic-ray (CR) nuclei from the second flight of the balloon-borne experiment Cosmic-Ray Energetics And Mass (CREAM). The instrument included different particle detectors to provide redundant charge identification and measure the energy of CRs up to several hundred TeV. The measured individual energy spectra of C, O, Ne, Mg, Si, and Fe are presented up to $\sim 10^{14}$ eV. The spectral shape looks nearly the same for these primary elements and it can be fitted to an $E^{-2.66\pm0.04}$ power law in energy. Moreover, a new measurement of the absolute intensity of nitrogen in the 100–800 GeV/n energy range with smaller errors than previous observations, clearly indicates a hardening of the spectrum at high energy. The relative abundance of N/O at the top of the atmosphere is measured to be $0.080 \pm 0.025\,(\text{stat.}) \pm 0.025\,(\text{sys.})$ at $\sim$800 GeV/n, in good agreement with a recent result from the first CREAM flight.

Key words: balloons – cosmic rays – instrumentation: detectors – ISM: abundances – methods: data analysis

1. INTRODUCTION

Experimental studies of charged cosmic rays (CRs) are focused on the understanding of the acceleration mechanism of high-energy CRs, identification of their sources, and clarification of their interactions with the interstellar medium (ISM). The origin of CRs is still under debate, although direct measurements with instruments on stratospheric balloons or in space have provided information on their elemental composition and energy spectra, and indirect detection by ground-based experiments has extended the measurements up to the end of the observed all-particle spectrum.

It is generally accepted that CRs are accelerated in blast waves of supernova remnants (SNRs), which are the only galactic candidates known with sufficient energy output to sustain the CR flux (Bell 1978; Hillas 2005). Recent observation of emission of TeV gamma rays from SNR RX J1713.7-3946 by the HESS Cherenkov telescope array proved that high-energy charged particles are accelerated in SNR shocks up to energies beyond 100 TeV (Aharonian et al. 2004). This result is consistent with expectations of the class of theoretical models that predict the existence of a rigidity dependent limit, above which the diffusive shock acceleration becomes inefficient. The maximum energy attainable by a nucleus of charge Z may range from $Z \times 10^{14}$ eV to $\sim Z \times 10^{17}$ eV depending on the model and types of supernovae considered (Lagage & Cesarsky 1983; Berezhko 1996; Parizot et al. 2004). In this scenario, the energy spectra of elements exhibit a Z-dependent cutoff. As a consequence, the CR elemental composition is expected to change as a function of energy, marked by a depletion of low-Z nuclei in the several hundred TeV region. This mechanism has been proposed as a possible explanation of the steepening ("knee") in the CR energy spectrum (described by a power law: $dN/dE \propto E^{-\gamma}$) with a change of the spectral index from $\gamma \approx 2.7$ to $\gamma \approx 3.1$, observed at energies around 4 PeV. An alternative approach is adopted by models that relate the knee to leakage of CRs from the Galaxy. In this case, the knee is expected to occur at lower energies for light elements as compared to heavy nuclei, due to the rigidity dependence of the Larmor radius of CR particles propagating in the galactic magnetic field (Hörandel 2004).

A detailed understanding of the propagation of CRs during their wanderings inside the Galaxy and their interactions with the ISM is needed to infer the injection spectra of individual elements at the source from the observed spectra at Earth. CR nuclei can be divided into primaries (i.e., H, He, C, O, Fe, etc.) that come from CR sources, and secondaries (such as Li, Be, B, Sc, Ti, V, etc.), which are products of the interactions of primary nuclei with the ISM. The amount of material traversed by CRs between injection and observation can be derived from the measured ratio of secondary-to-primary nuclei, such as the boron-to-carbon ratio (B/C) or the ratio of sub-iron elements to iron. Likewise, their confinement time in the Galaxy can be determined through measurements of long-lived radioactive secondary nuclei (Longair 1994; Yanasak et al. 2001). Observations from space-based experiments like cosmic ray nuclei (CRN) on the Spacelab2 mission of the Space Shuttle (Swordy et al. 1990) and C2 (Engelman et al. 1990) and Heavy Nuclei Experiment (HNE; Binns et al. 1988) onboard the *HEAO 3* satellite have shown that the energy spectra of the secondary nuclei are steeper than those of the primaries. The escape path

[11] Corresponding author: paolo.maestro@pi.infn.it

length of CRs from the Galaxy depends on the magnetic rigidity as $R^{-\delta}$, with the parameter $\delta \approx 0.6$. This implies that the spectra observed at Earth are steeper than the injection spectra, i.e., the spectral index at the source is smaller by the value δ.

Those pioneering measurements were statistically limited at energies of order $\sim 10^{11}$ eV. Accurate direct measurements of the energy spectra of individual elements into the knee region are needed to discriminate between different astrophysical models proposed to explain the acceleration and propagation mechanisms. Recently, a new generation of balloon-borne experiments has performed accurate measurements of CRs in the previously experimentally unexplored TeV region (Panov et al. 2006; Ave et al. 2008). Among these, the Cosmic Ray Energetics And Mass (CREAM) experiment was designed to measure directly the elemental composition and the energy spectra of CRs from hydrogen to iron over the energy range 10^{11}–10^{15} eV in a series of flights (Seo et al. 2004). Since 2004, four instruments were successfully flown on long-duration balloons in Antarctica. The instrument configurations varied slightly in each mission due to various detector upgrades. The first flight produced important results extending the measurement of the relative abundances of CR secondary nuclei B and N close to the highest energies ($\sim$1.5 TeV/n) allowed by the irreducible background generated by the residual atmospheric overburden at balloon altitudes. The data clearly indicate that the escape path length of CRs from the Galaxy has a power-law rigidity-dependence, with the parameter δ in the range 0.5–0.6 (Ahn et al. 2008).

In this work, we present new measurements of the energy spectra of the major primary CR nuclei from carbon to iron, up to a few TeV/n made with the second CREAM flight (CREAM-II). A new measurement of the nitrogen intensity with unprecedented statistics is also presented up to 800 GeV/n. The measured N/O ratio confirms the results of CREAM-I. The procedure used to analyze the data and reconstruct the CR energy spectra is described in detail together with an assessment of the systematic uncertainties.

2. THE CREAM-II INSTRUMENT

The instrument for the second flight included: a redundant system for particle identification, consisting (from top to bottom) of a timing-charge detector (TCD), a Cherenkov detector (CD), a pixelated silicon charge detector (SCD), and a sampling imaging calorimeter (CAL) designed to provide a measurement of the energy of CR nuclei in the multi-TeV region. Figure 1 depicts the detector arrangement.

The TCD is made of two orthogonal layers of four 5 mm thick plastic scintillator paddles each, covering an area of 120 $\times$ 120 cm^2. The paddles are read out by fast photomultiplier tubes (PMTs) via twisted-strip adiabatic light guides. A custom design of the electronics combines fast peak detection with a threshold timing measurement of the PMTs signals in order to determine each element's charge with a resolution $\lesssim$0.35 e (in units of the electron charge) and to discriminate against albedo particles. A hodoscope (S3) of 2 $\times$ 2 mm^2 square scintillating fibers read out by two PMTs is located just above the calorimeter, and provides a reference time for TCD timing readout. Further details about the TCD design and performance can be found in Ahn et al. (2009). The CD is a 1 cm thick plastic radiator with 1 m^2 surface area, instrumented with eight PMTs viewing wavelength shifting bars placed along the radiator edges. It is used to flag relativistic particles and to provide a charge determination complementary to that of the TCD.

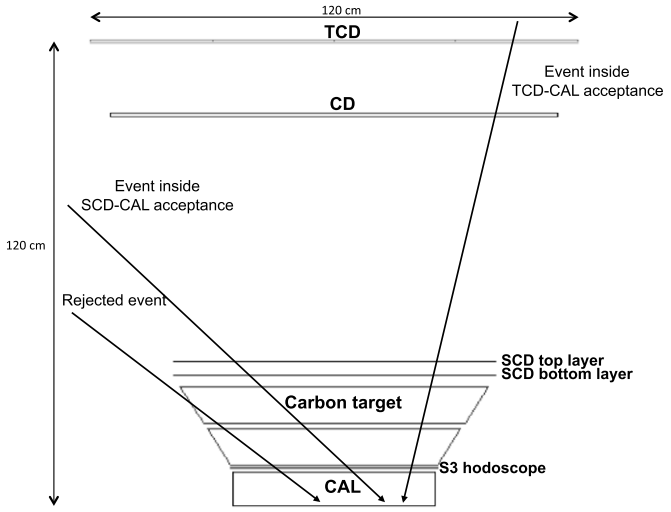

Figure 1. Schematic view of the CREAM-II instrument.

The SCD is comprised of two layers of 156 silicon sensors each. Each 380 μm thick sensor is segmented into an array of 4 $\times$ 4 pixels, each of which has an active area of 2.12 cm^2 (Park et al. 2007). The sensors are slightly tilted and overlap each other in both lateral directions, providing a full coverage in a single layer, with a 77.9 $\times$ 79.5 cm^2 area. The dual layers, about 4 cm apart, cover an effective inner area of 0.52 m^2 with no insensitive regions. The overall SCD vertical dimension, including the ladders, the mechanical support structure and the electromagnetic shielding cover, is 97.5 mm (Nam et al. 2007). The readout electronics of the 4992 pixels is based on a 16-channel ASIC chip followed by 16-bit analog-to-digital converters (ADCs), providing a fine charge resolution over a wide dynamic range from hydrogen to nickel.

The CAL is a stack of 20 tungsten plates, each 1 radiation length (X_0) thick and with surface area 50 $\times$ 50 cm^2, interleaved with active layers of 1 cm wide and 50 cm long scintillating-fiber ribbons. Each ribbon is built by gluing together 19 scintillating fibers of 0.5 mm diameter each. The light signal from each ribbon is collected by means of an acrylic light mixer coupled to a bundle of 48 clear fibers. This is split into three sub-bundles (with 42, 5 and 1 fibers, respectively), each feeding a pixel of a hybrid photodiode (HPD). This optical division is used to match the wide dynamic range of the calorimeter to that of the front-end electronics, providing three readout scales (low, medium, and high) with different sensitivity. A total of 2560 channels are readout from 40 HPDs powered in groups of 5 units.

The longitudinal and lateral segmentations of the CAL correspond to 1 X_0 and 1 Moliere radius, respectively. The ribbon planes are alternately oriented along orthogonal directions to image in three dimensions, the development of showers produced by the incoming nuclei which interact inelastically in the $\sim$0.46 $\lambda_{\rm int}$ thick carbon target preceding the CAL (Marrocchesi et al. 2004). The finely grained sampling calorimeter can track, by reconstructing the shower axis, the incident particle trajectory with enough accuracy to determine which segment of each charge detector it traversed, and thereby allowing discrimination against segments hit by the backscattered particles produced in the shower. This feature is essential for a reliable and unambiguous charge identification.

3. BALLOON FLIGHT AND INSTRUMENT PERFORMANCE

The second CREAM instrument was launched from McMurdo station in Antarctica on 2005 December 16th. The balloon circled the South Pole twice at a float altitude between 35 and 40 km. The flight was terminated on 2006 January 13th, 28 days after the launch. During the whole flight, the instrument housekeeping system monitored online temperatures, currents, voltages of the front-end electronics boards, and the high-voltage supply values of the HPDs and PMTs. The performance of all sub-detectors met the design technical specifications. The CAL and TCD high-voltage systems worked successfully at low atmospheric pressure. The thermal behavior of the various detectors was found to be in good agreement with expectations from thermal models. The temperature of the instrument crates stayed within the required operational range with daily variation of a few °C, depending on the inclination of the Sun during each 24 hr cycle. Front-end electronics channels showed stable gains over the whole flight. Pedestal values of the 2560 CAL and 4992 SCD channels were collected automatically every 5 minutes in order to monitor their drift as a function of the detector temperature and to perform accurate pedestal subtraction. 1.7% of the SCD and 0.7% of the CAL channels were noisy or inefficient and were masked off.

During the flight, the data acquisition was enabled whenever a shower developing in at least six planes was detected in the CAL (CAL trigger) and/or a relativistic CR with $Z \geqslant 2$ was identified by the TCD and CD (TCD trigger). The high-energy data, i.e., the CAL triggered events, were transmitted via Tracking and Data Relay Satellite System (TRDSS), while the low-energy data, i.e., events triggered only by the TCD and not by the CAL, were recorded on an onboard disk. A total of 57 GB of data were collected. In order not to saturate the disk space too early in the flight, the highly abundant low-energy particles triggered only by the TCD were pre-scaled, so that only a fraction of these events were recorded. This fraction of recorded TCD triggers (pre-scale factor) could be set by the data acquisition program and changed during the flight depending on the trigger rate. On average, only one every six TCD triggered events was retained. A detailed description of the instrument performance during the second flight may be found in Marrocchesi et al. (2008).

4. DATA ANALYSIS

The present analysis uses a subset of data collected from December 19th to January 12th, under stable instrument conditions, representing a total of 24 days' worth of data taking (e.g., removing periods early in the flight and at the very end, when the instrument was either being adjusted and optimized, or prepared for flight termination). The first step in the analysis is to correct the raw data for the gain variations among the channels and the drift of the pedestals with temperature. Then, the trajectory of each CR through the instrument is reconstructed and each event assigned a charge and an energy. At this point, the events of each charge species are sorted into energy intervals and the number of counts in each bin is corrected for several effects in order to compute the differential intensity. The various steps of the analysis procedure are described in detail in the following subsections.

4.1. Trajectory Reconstruction

To determine the arrival direction of a CR, the axis of the shower imaged by the calorimeter is measured with the following method. In each CAL plane, an offline software algorithm searches for clusters of adjacent cells with pulse heights larger than a threshold value, corresponding to an energy deposit of about 10 MeV. The cluster formed by the cell with the maximum pulse height and its two neighbors defines a candidate track point. Its coordinates are computed as the center of gravity of the cluster. A track is formed by matching at least three candidate track points sampled in each CAL view. The shower axis parameters are calculated by a linear χ^2 fit of the track. Track quality is assured by requiring a value of $\chi^2 < 10$. The reconstructed shower axis is projected back to the top of the instrument (TOI) in order to determine which SCD pixels and TCD paddles were hit by the incoming CR. Particles showering in the CAL, but crossing neither the TCD scintillator paddles nor the SCD planes are rejected. Otherwise, if the particle crosses the SCD, a circle of confusion with a 3 cm radius centered on the impact point of the track is traced in each SCD layer. The value of the radius is equal to about three times the estimated uncertainty on the impact point. The hit pixels within each circle of confusion are scanned and the pixel with the maximum pulse height is selected for the charge assignment procedure. In order to improve the trajectory determination and the accuracy of the path length correction, the two selected pixels, one per SCD layer, are added to the candidate points and the track is fitted again. In this way, the intersection of the particle trajectory with the top SCD layer is measured with a spatial resolution of 7 mm rms. The incidence direction is determined with an accuracy of better than 1° as estimated with Monte Carlo (MC) simulations.

This procedure reconstructs well the trajectories of over 95% of the CR particles with energy >3 TeV triggered by the CAL. It can also identify the TCD triggered events which produce a shower in the CAL, but with an energy release insufficient to satisfy the CAL trigger condition.

4.2. Charge Assignment

The identification of the charge Z of a CR relies on two independent samples of its specific ionization dE/dx provided by the SCD layers. Since dE/dx depends on Z^2 and for solid absorbers it is nearly constant in the relativistic regime, the particle charge Z can be determined by measuring the amount of ionization charge a CR produces when traversing the silicon sensors. In order to avoid charge misidentification of the incident nucleus, caused by the backscattered shower particles reaching the SCD, and to obtain high-purity samples of CR elements, the signals, $S_{\rm top}$ and $S_{\rm bottom}$, of the two pixels selected by the tracking algorithm are compared and required to be consistent within 20%. If this coherence cut is satisfied, they are corrected for the path length (estimated from the track parameters) traversed by the particle in the silicon sensors, which is proportional to $1/\cos(\theta)$, θ being the angle between the particle trajectory and the axis of the instrument. A reconstructed charge $Z_{\rm rec}$ is assigned to the particle by combining the ionization signals matched with the track on both layers, according to the formula

$$Z_{\rm rec} = \sqrt{\frac{S_{\rm top} + S_{\rm bottom}}{2} \times \frac{\cos(\theta)}{s_0}}, \qquad (1)$$

where s_0 is a calibration constant, inferred from the flight data, to convert the pulse heights into an absolute charge scale. The reconstructed charge distribution is shown in Figure 2. The elemental range from boron to silicon is fitted with a multi-Gaussian function (Figure 2(a)). From the fit, a charge resolution σ is estimated as: $0.2e$ for C, N, O and $\sim 0.23e$ for Ne, Mg,

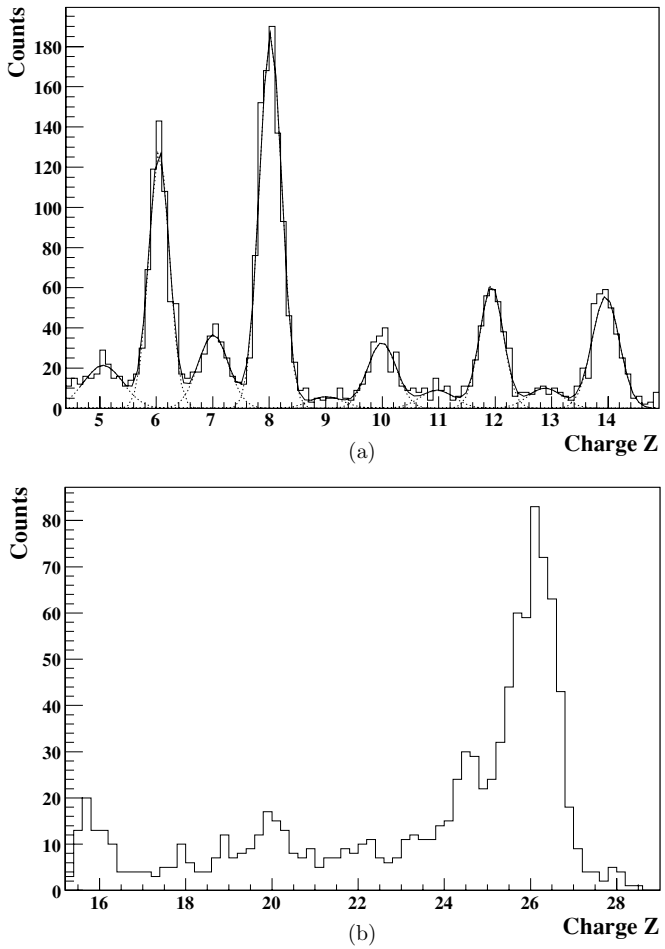

Figure 2. Charge histogram obtained by the SCD in the elemental range (a) from boron to silicon and (b) from sulfur to nickel. The distributions are only indicative of the SCD charge resolution and the relative elemental abundances are not meaningful. The peaks from B to Si are fitted to a multi-Gaussian function.

Si. Though a multi-Gaussian fit in the elemental region from sulfur to nickel cannot be done due the limited statistics, the charge resolution for iron is estimated to be $\sim 0.5e$ from the width of the Fe peak. A 2σ cut around the mean charge value is applied to select samples of C, O, Ne, Mg, and Si. A cut of $Z_{\rm rec} \pm 1\sigma$ is imposed for Fe due to the corresponding lower SCD resolution, while for N a cut of $Z_{\rm rec} \pm 1.5\sigma$ and 10% coherence level between the selected pixels signals, are used to avoid contamination from more abundant adjacent charges.

4.3. Energy Measurement

Due to the limitations on mass and size imposed to the payload, a balloon-borne experiment cannot employ a total containment hadronic calorimeter to measure the energy of CR nuclei. An alternative and workable technique is to use a thin ionization calorimeter to sample the electromagnetic core of the hadronic cascade initiated by a CR interacting in a target preceding the calorimeter. In fact, though a significant part of the hadronic cascade energy leaks out of the calorimeter, the energy deposited in the calorimeter by the shower core still scales linearly with the incident particle energy, albeit with large event-to-event fluctuations. As a result, the energy resolution is poor by the standards of hadron calorimetry in experiments at accelerators. Nevertheless, it is sufficient to reconstruct the steep energy spectra of CR nuclei with a nearly energy independent resolution.

The CREAM calorimeter was designed to measure CRs over a wide energy range, from tens of GeV up to about 1 PeV. It is characterized by a very small sampling fraction; only about 0.1% of the CR energy is converted into visible signals in the CAL active planes and collected by the photosensors. Three different gain scales (low, medium, and high) were implemented for each ribbon in order to prevent saturation of the readout electronics and thereby to ensure a linear detector response up to very high energies.

The total energy deposited in the calorimeter by an interacting nucleus, is measured by summing up the corrected pulse heights of all the cells. The cells are equalized for non-uniformity in light output and gain differences among the photodetectors using a set of calibration constants from accelerator beam tests (described below), scaled according to the high-voltage settings during the flight. Low and medium gain scales are inter-calibrated using the flight data; the medium-range signal of each ribbon is used whenever the corresponding low-range signal deviates from linearity due to saturation.

The CREAM calorimeter was tested, equalized, and calibrated pre-flight at the CERN SPS accelerator with beams of electrons and protons up to a few hundred GeV (Ahn et al. 2004). Its response to relativistic nuclei was also studied by exposing the calorimeter to nuclear fragments from a 158 GeV/n primary indium beam. The detector was found to have a linear response up to the maximum beam energy, equivalent to about 8.2 TeV particle energy, and a nearly flat resolution (around 30%), at energies above 1 TeV for all heavy nuclei with $Z \geqslant 5$ (Ahn et al. 2006). Above the maximum beam energy, the calorimeter response was extrapolated using MC simulations, which predict a linear behavior up to hundreds of TeV.

4.4. Energy Deconvolution

Once each CR is assigned a charge and energy, the reconstructed particles of each nuclear species are sorted into energy intervals commensurate with the rms resolution of the calorimeter. Due to the finite energy resolution of the detector, the measured number of events in each energy bin must be corrected for overlap with the neighboring bins. This unfolding procedure requires solving a set of linear equations

$$M_i = \sum_{j=1}^{n} A_{ij} N_j \qquad i = 1, ..., m \tag{2}$$

relating the "true" counts N_j in one of n incident energy bins to the measured counts M_i in one of m deposited energy bins. A generic element of the mixing matrix A_{ij} represents the probability that a CR particle, carrying an energy corresponding to a given energy bin j, produces an energy deposit in the calorimeter falling into bin i instead. A detailed MC simulation of the instrument, based on the FLUKA 2006.3b package (Fassò et al. 2005), was developed to estimate the unfolding matrix. Sets of nuclei, generated isotropically and with energies chosen according to a power-law spectrum, are analyzed with the same procedure used for the flight data. Each matrix element A_{ij} is calculated by correlating the generated spectrum with the distribution of the deposited energy in the calorimeter (Zei et al. 2008). In order to get a reliable set of values of the unfolding matrix for each nucleus, the MC simulation is finely tuned to reproduce both flight data and the calibration data

collected with accelerated particle beams. The agreement of the MC description with the real instrument behavior was carefully checked. As an example, in Figure 3 the response of the calorimeter to carbon nuclei from the flight data is compared with an equivalent set of simulated events.

The elements of the unfolding matrix depend on the spectral index assumed for the generation of MC events. For each nucleus, we used the spectral index value reported by Hörandel (2003), obtained by combining direct and indirect CR observations. In order to check the stability of our final results, the unfolding procedure was repeated by scanning several values of the spectral index in the range ± 0.2 around the reference value. No significant bias of the final results was observed.

4.5. Corrections for Interactions in the Atmosphere and the Detector

CRs may undergo spallation reactions when traveling through the atmosphere above the balloon or crossing the instrument material of CREAM above the SCD. This results in the generation of secondary nuclei with lower charge than the parent's, and of about the same energy per nucleon. Then, for each nuclear species, inelastic interactions lead to a loss of primary particles but also a gain of secondaries produced by heavier nuclei. For a correct determination of the CR fluxes, the data must be corrected for this effect. A two-step procedure is used which takes into account separately the CR path length in air (correction to the top of the atmosphere (TOA)) and the amount of instrument material encountered by the particle before reaching the SCD. The latter leads to a correction to the TOI. For each step, the corrections are calculated by solving the matrix equation

$$\begin{pmatrix} N_{\rm C} \\ N_{\rm N} \\ N_{\rm O} \\ N_{\rm Ne} \\ N_{\rm Mg} \\ N_{\rm Si} \\ N_{\rm Fe} \end{pmatrix}_{\mathcal{F}} = \begin{pmatrix} S_{\rm C} & F_{\rm N\to C} & F_{\rm O\to C} & F_{\rm Ne\to C} & F_{\rm Mg\to C} & F_{\rm Si\to C} & F_{\rm Fe\to C} \\ 0 & S_{\rm N} & F_{\rm O\to N} & F_{\rm Ne\to N} & F_{\rm Mg\to N} & F_{\rm Si\to N} & F_{\rm Fe\to N} \\ 0 & 0 & S_{\rm O} & F_{\rm Ne\to O} & F_{\rm Mg\to O} & F_{\rm Si\to O} & F_{\rm Fe\to O} \\ 0 & 0 & 0 & S_{\rm Ne} & F_{\rm Mg\to Ne} & F_{\rm Si\to Ne} & F_{\rm Fe\to Ne} \\ 0 & 0 & 0 & 0 & S_{\rm Mg} & F_{\rm Si\to Mg} & F_{\rm Fe\to Mg} \\ 0 & 0 & 0 & 0 & 0 & S_{\rm Si} & F_{\rm Fe\to Si} \\ 0 & 0 & 0 & 0 & 0 & 0 & S_{\rm Fe} \end{pmatrix} \times \begin{pmatrix} N_{\rm C} \\ N_{\rm N} \\ N_{\rm O} \\ N_{\rm Ne} \\ N_{\rm Mg} \\ N_{\rm Si} \\ N_{\rm Fe} \end{pmatrix}_{\mathcal{I}}, \quad (3)$$

which describes the transport process of the nuclei from an incident level $\mathcal{I}$ (e.g., TOI) to a final level $\mathcal{F}$ (e.g., the SCD). The vector $\mathbf{N}_{\mathcal{I}}$ represents the number of nuclei of each species counted in a given energy interval, while the vector $\mathbf{N}_{\mathcal{F}}$ is the number of counts corrected for the charge-changing interactions in the materials between the levels $\mathcal{I}$ and $\mathcal{F}$. The diagonal elements of the transport matrix represent the survival probabilities of each species Z in the passage from $\mathcal{I}$ to $\mathcal{F}$, while a generic off-diagonal element $F_{Z_2\to Z_1}$ gives the fraction of nuclei Z_2 which spallate to produce nuclei of charge Z_1 ($< Z_2$).

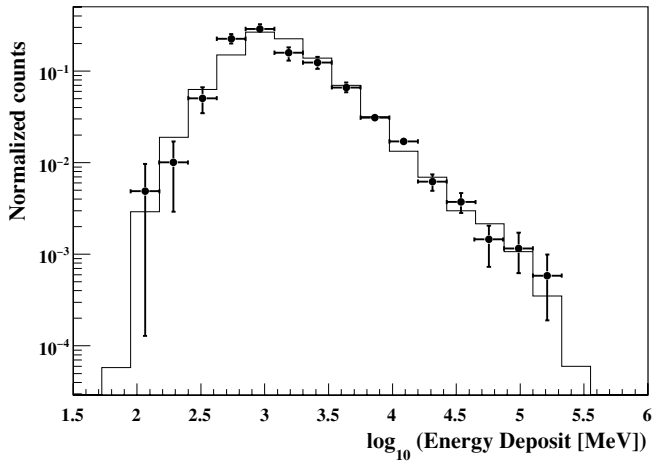

Figure 3. Energy deposited in the calorimeter by a selected sample of carbon nuclei. Simulated (histogram) and real (dots) events are shown.

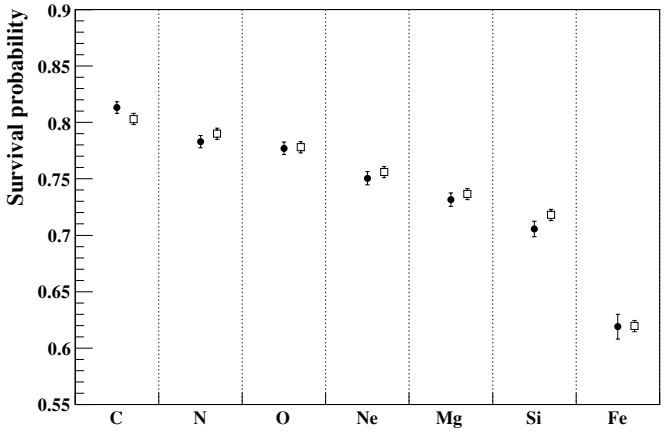

Figure 4. Survival probabilities of CR nuclei traversing the materials between the TOI and the upper SCD layer. For each elemental species, the correction is estimated in two different ways: (filled circles) from the FLUKA-based (Fassò et al. 2005) Monte Carlo simulation of the CREAM-II instrument; (open squares) from calculations using the semiempirical total cross section formulae for nucleus–nucleus reactions developed by Sivher et al. (1993).

The TOI transport matrix is obtained from the MC simulation of the instrument. The mass thickness of the CREAM-II materials above the SCD is estimated to be $\sim$4.8 g cm^{-2}. The fraction of surviving nuclei, i.e., the diagonal matrix elements, ranges from 81.3% for C to 61.9% for Fe. These MC values are compared with the ones calculated using the semiempirical total cross section formulae for nucleus–nucleus reactions given in Sivher et al. (1993). Good agreement, within 1%, is found as shown in Figure 4.

The TOA matrix elements are calculated by simulating with FLUKA the atmospheric overburden during the flight (3.9 g cm^{-2} on average). Since the probability of interaction depends on the nucleus path length in air, the simulated events are generated according to the measured zenith angle distribution of the reconstructed nuclei, which is peaked around 20°. Survival probabilities ranging from 84.2% for C to 71.6% for Fe are found (Figure 5). They turn out to be in good agreement with the values calculated from two different empirical parameterizations (Sivher et al. 1993; Kox et al. 1987) of the total fragmentation cross sections of heavy relativistic nuclei in targets of different mass.

The off-diagonal elements $F_{Z_2\to Z_1}$ of both the TOI and TOA transport matrices are of order 1%–2%. The comparison

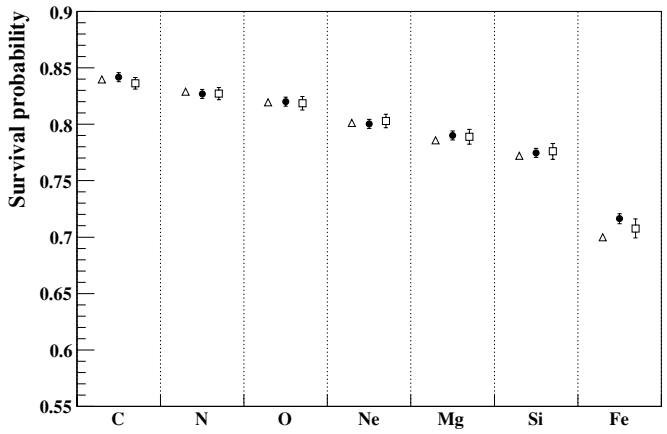

Figure 5. Survival probabilities of nuclei in a residual atmospheric overburden of 3.9 g cm^{-2}. For each elemental species, three values of the same correction are shown, obtained respectively from the FLUKA-based (Fassò et al. 2005) Monte Carlo simulation of the CREAM-II instrument (filled circles), and from calculations using two different parameterizations of the total fragmentation cross sections for nucleus–nucleus reactions: Sivher et al. (1993; open squares); Kox et al. (1987; open triangles).

between values obtained from different models is discussed in Section 5.1.

4.6. Absolute Differential Intensity Calculation

The absolute differential intensity dN/dE at an energy $\hat{E}$ is calculated for each elemental species according to the formula

$$\frac{dN}{dE}(\hat{E}_i) = \frac{\tilde{N}_i}{\Delta E_i} \times \frac{1}{\epsilon \times S\Omega \times T}, \quad (4)$$

where $\tilde{N}_i$ is the number of events obtained from the unfolding algorithm and corrected to the TOA, ΔE_i is the energy bin width, T is the exposure time, $S\Omega$ the geometric factor of the instrument, and ϵ the efficiency of the analysis selection. Since a significant fraction of the reconstructed events at energies, <3 TeV did not satisfy the CAL trigger condition and were triggered only by the TCD, the number of these events in the first energy intervals must be further divided by the pre-scale factor (1/6 on average during the flight) of the TCD-based trigger system.

Median energy. According to the work of Lafferty & Wyatt (1995), each data point, i.e., each differential intensity value, is centered at a median energy $\hat{E}$, defined as the energy at which the measured spectrum is equal to the expectation value of the "true" spectrum. For a power-law spectrum ($E^{-\gamma}$) with spectral index γ, the median energy is calculated as

$$\hat{E} = \left[\frac{E_2^{1-\gamma} - E_1^{1-\gamma}}{(E_2 - E_1)(1-\gamma)} \right]^{-\frac{1}{\gamma}}, \quad (5)$$

where E_1 and E_2 are the lower and upper limits of a given energy bin. If the highest energy interval is not limited, i.e., $E_2 \to \infty$, the median energy is $\hat{E} = 2^{\frac{1}{\gamma-1}} E_1$. In this case, the energy interval is an integral bin and its width (to be used in Equation (4)) is calculated as

$$\Delta E = \frac{E_1}{2^{\frac{\gamma}{1-\gamma}}(\gamma - 1)}. \quad (6)$$

Since γ is not known a priori, an iterative procedure is performed to compute the median energy of each bin. For each element, the spectral index reported by Hörandel (2003) is used as the initial value of γ. We found that $\hat{E}$ depends weakly on γ for a variation of ± 0.1 around the initial value.

Geometric factor. The geometric factor $S\Omega$ is estimated from MC simulations by counting the fraction of generated particles entering the trigger-sensitive part of instrument. Two groups of events are distinguished as shown in Figure 1: CRs crossing both the TCD and the SCD before impinging onto the CAL (named "golden" events), and particles entering the instrument through the side (i.e., crossing neither the TCD nor the CD) and traversing only the SCD and the CAL. The estimated acceptance is (0.19 ± 0.01) m^2 sr in the first case, while including both event types yields a value of (0.46 ± 0.01) m^2 sr. Both values are charge and energy independent. For the second group of events, the corrections to the TOI are not necessary.

Live Time. During the flight, the total time and the live time T (i.e., the time during which the data acquisition was available for triggers) were measured by means of a pair of 48 bit counters incorporated in the housekeeping system onboard, and providing better than 4 microseconds resolution. The selected data set amounts to a live time of 1,454,802 seconds, close to 75% of the total time of data taking.

Reconstruction efficiency. The overall efficiency ϵ, including the trajectory reconstruction and the charge selection efficiencies, is estimated from MC simulations as a function of the particle energy. This efficiency curve is characterized by a steep rise below 2 TeV and reaches a constant value at energies >3 TeV for all nuclei. The rise is caused by the high sparsification threshold (∼10 MeV) of the CAL cells, which limits the CAL tracking accuracy at low energy and consequently the charge identification capability of the instrument. For C, O, Ne, Mg, and Si, the plateau value in the efficiency curve is about 80% when considering only the "golden" events, and decreases to 65% when including also events at large angle within the SCD–CAL acceptance. Instead, the more conservative charge cuts applied to select N and Fe samples (see Section 4.2) yield a reduced plateau efficiency of about 65% and 35% (for "golden" events), respectively.

5. RESULTS

The differential intensities at the TOA as measured by CREAM-II for the elements C, N, O, Ne, Mg, Si, and Fe are given as a function of the kinetic energy per nucleon in Table 1, together with the corresponding number of raw observed particles. The quoted error bars are due to the counting statistics only: the upper and lower limits are computed as 84% confidence limits for Poisson distributions as described by Gehrels (1986).

The energy spectra of the major primary CR nuclei from carbon to iron are plotted as a function of the kinetic energy per particle in Figure 6. To emphasize the spectral differences, the differential intensities are multiplied by $\hat{E}^{2.5}$ and plotted as a function of the kinetic energy per nucleon in Figure 7. The error bars shown in the figures represent the sum in quadrature of the statistical and systematic uncertainties. The assessment of systematics is discussed in detail in the following section. The particle energy range covered by CREAM-II extends from around 800 GeV up to 100 TeV. The absolute intensities are presented without any arbitrary normalization to previous data and cover a range of six decades.

The energy spectrum of nitrogen is shown in Figure 8. The statistical and systematic errors in the differential intensity are

Table 1
Differential Intensities Measured with CREAM-II

Element	Energy Range (GeV/n)	Kinetic Energy $\hat{E}$ (GeV/n)	No. of Events	Intensity $(\mathrm{m^2\ sr\ s\ GeV}/n)^{-1}$
C	66–117	86.2	171	$(1.67 \pm 0.13) \times 10^{-4}$
$Z = 6$	117–175	141.6	139	$(3.37 \pm 0.29) \times 10^{-5}$
	175–304	228.2	215	$(9.42 \pm 0.64) \times 10^{-6}$
	304–529	397.2	134	$(2.28 \pm 0.20) \times 10^{-6}$
	529–919	691.0	66	$(5.17 \pm 0.63) \times 10^{-7}$
	919–1597	1201.5	29	$(1.31 \pm 0.24) \times 10^{-7}$
	1597–2776	2088.7	13	$(3.6\ ^{+1.3}_{-1.0}) \times 10^{-8}$
	2776–4824	3630.5	7	$(1.04\ ^{+0.58}_{-0.40}) \times 10^{-8}$
	4284–	7415.1	5	$(1.49\ ^{+0.98}_{-0.63}) \times 10^{-9}$
N	56–175	95.7	86	$(7.28 \pm 0.79) \times 10^{-6}$
$Z = 7$	175–529	295.3	63	$(5.39 \pm 0.68) \times 10^{-7}$
	529–	826.3	19	$(3.8\ ^{+1.1}_{-0.9}) \times 10^{-8}$
O	49–87	64.0	224	$(3.48 \pm 0.23) \times 10^{-4}$
$Z = 8$	87–175	120.8	371	$(4.82 \pm 0.25) \times 10^{-5}$
	175–304	228.0	241	$(7.33 \pm 0.47) \times 10^{-6}$
	304–529	396.9	127	$(1.90 \pm 0.17) \times 10^{-6}$
	529–919	690.5	57	$(4.51 \pm 0.60) \times 10^{-7}$
	919–1597	1200.5	25	$(1.25 \pm 0.25) \times 10^{-7}$
	1597–2776	2087.0	10	$(2.9\ ^{+1.2}_{-0.9}) \times 10^{-8}$
	2776–4824	3627.4	6	$(8.3\ ^{+4.9}_{-3.3}) \times 10^{-9}$
	4284–	7287.1	3	$(8.4\ ^{+9.7}_{-5.4}) \times 10^{-10}$
Ne	40–58	47.0	37	$(1.20 \pm 0.20) \times 10^{-4}$
$Z = 10$	58–101	74.8	65	$(2.59 \pm 0.32) \times 10^{-5}$
	101–175	130.7	67	$(5.53 \pm 0.68) \times 10^{-6}$
	175–304	227.9	36	$(1.06 \pm 0.18) \times 10^{-6}$
	304–529	396.7	19	$(2.86\ ^{+0.84}_{-0.66}) \times 10^{-7}$
	529–919	690.0	8	$(6.5\ ^{+3.1}_{-2.2}) \times 10^{-8}$
	919–1597	1199.8	4	$(1.8\ ^{+1.4}_{-0.9}) \times 10^{-8}$
	1597–2776	2085.6	2	$(3.7\ ^{+5.6}_{-2.0}) \times 10^{-9}$
	2776–	4150.9	3	$(2.2\ ^{+2.1}_{-1.2}) \times 10^{-9}$
Mg	20–40	27.0	48	$(4.68 \pm 0.67) \times 10^{-4}$
$Z = 12$	40–58	47.0	45	$(1.07 \pm 0.16) \times 10^{-4}$
	58–101	74.9	103	$(2.91 \pm 0.29) \times 10^{-5}$
	101–175	130.8	94	$(5.41 \pm 0.56) \times 10^{-6}$
	175–304	228.0	51	$(1.42 \pm 0.20) \times 10^{-6}$
	304–529	397.0	26	$(3.72 \pm 0.73) \times 10^{-7}$
	529–919	690.6	12	$(8.5\ ^{+3.3}_{-2.4}) \times 10^{-8}$
	919–1597	1200.8	4	$(1.9\ ^{+1.6}_{-1.0}) \times 10^{-8}$
	1597–2776	2087.5	3	$(6.7\ ^{+7.1}_{-4.0}) \times 10^{-9}$
	2776–	4215.9	1	$(6.0\ ^{+16.0}_{-5.8}) \times 10^{-10}$
Si	20–40	27.0	66	$(4.54 \pm 0.56) \times 10^{-4}$
$Z = 14$	40–58	47.0	64	$(1.35 \pm 0.17) \times 10^{-4}$
	58–101	74.9	116	$(3.03 \pm 0.28) \times 10^{-5}$
	101–175	130.8	89	$(5.04 \pm 0.53) \times 10^{-6}$
	175–304	228.0	54	$(1.50 \pm 0.20) \times 10^{-6}$
	304–529	397.0	24	$(3.88 \pm 0.79) \times 10^{-7}$
	529–919	690.6	10	$(1.15\ ^{+0.48}_{-0.35}) \times 10^{-7}$
	919–1597	1200.7	3	$(1.9\ ^{+1.7}_{-0.9}) \times 10^{-8}$
	1597–	2418.3	2	$(3.2\ ^{+3.6}_{-1.8}) \times 10^{-9}$
Fe	18–40	25.4	108	$(5.19 \pm 0.56) \times 10^{-4}$
$Z = 26$	40–58	47.0	88	$(8.38 \pm 0.89) \times 10^{-5}$
	58–101	74.9	70	$(2.06 \pm 0.25) \times 10^{-5}$
	101–175	131.0	27	$(4.46 \pm 0.85) \times 10^{-6}$
	175–304	228.2	15	$(1.36\ ^{+0.46}_{-0.36}) \times 10^{-6}$
	304–529	397.2	9	$(4.0\ ^{+1.8}_{-1.3}) \times 10^{-7}$
	529–919	690.9	4	$(1.09\ ^{+0.79}_{-0.48}) \times 10^{-7}$
	919–	1406.9	4	$(1.6\ ^{+1.4}_{-0.8}) \times 10^{-8}$

shown separately to point out that the systematic uncertainties from the corrections for secondary particle production in the atmosphere and the instrument, are particularly relevant for this measurement. In practice, they impose a limit on the maximum energy at which measurements of nitrogen in CRs might be pursued on a balloon flight.

The elemental abundances with respect to oxygen are calculated from the differential intensities at the TOA and are shown as a function of energy in Figure 9. Energy bins at high energy are merged together in order to reduce the statistical error in the ratio to an acceptable level.

5.1. Estimate of the Systematic Errors

The main systematic uncertainties in the differential intensity stem from the reconstruction algorithm as well as from the TOI and TOA corrections. To estimate the first, we scan a range of thresholds around the reference value of each selection cut and derive the corresponding fluxes. In particular, the analysis procedure has been repeated by varying the fiducial area of the SCD and CAL, the coherence level between the signals of the SCD pixels crossed by the CR particle, and the limits of charge selection cut for each element. Comparing the results with the reference, a systematic fractional error in the differential intensity, arising from the reconstruction procedure, is estimated to be of order 10% below a particle energy of 3 TeV and 5% above.

The second source of systematic errors comes from the uncertainties in the nucleus–nucleus charge-changing cross sections used to calculate the instrument and atmospheric corrections. While there is a general agreement between different parameterizations of the total cross sections, leading to very similar values of the survival fractions of CRs in the atmosphere and in the instrument (Figures 4 and 5), the partial charge-changing cross sections reported in the literature are measured with quoted errors of order 10%–15%, depending on the specific nucleus–nucleus interaction, and can differ by up to ∼30%. This may result in significantly different values of the off-diagonal elements $F_{Z_2 \to Z_1}$ in the transport matrix. For instance, the values we calculated for the fraction of oxygen nuclei which spallate in the atmosphere producing nitrogen nuclei ($F_{\mathrm{O} \to \mathrm{N}}$), are respectively: 1.7% from the partial cross-section model of Tsao et al. (1993); 1.9% according to the parameterization of Nilsen et al. (1995); 1.5% from FLUKA (Fassò et al. 2005). In order to estimate how these uncertainties in the corrections for secondary nuclei production in the atmosphere and the instrument affect our final results, we developed the following method. Using the same sample of analyzed data for each element, we varied the values of the charge-changing probabilities in the range allowed by the different models and derived, for each set of values, the corresponding energy spectrum. By comparing the results with the reference spectrum, the systematic error for the uncertainty in correcting the differential intensity to the top of instrument is estimated to be 2% for the primary elements. For nitrogen, a 15% error is assigned because of the large contamination of O nuclei which spallate into N. Similar values are estimated for the systematic error from the uncertainties in the atmospheric secondary corrections.

The systematic error in the energy scale, as measured by the CAL, derives from the accuracy with which the simulated CAL response corresponds to the real behavior of the calorimeter at energies not covered by beam test measurements. We estimate this accuracy at a 5% level, which corresponds, given the CAL linearity in the energy range considered in this work, to an energy-scale uncertainty of 5%.

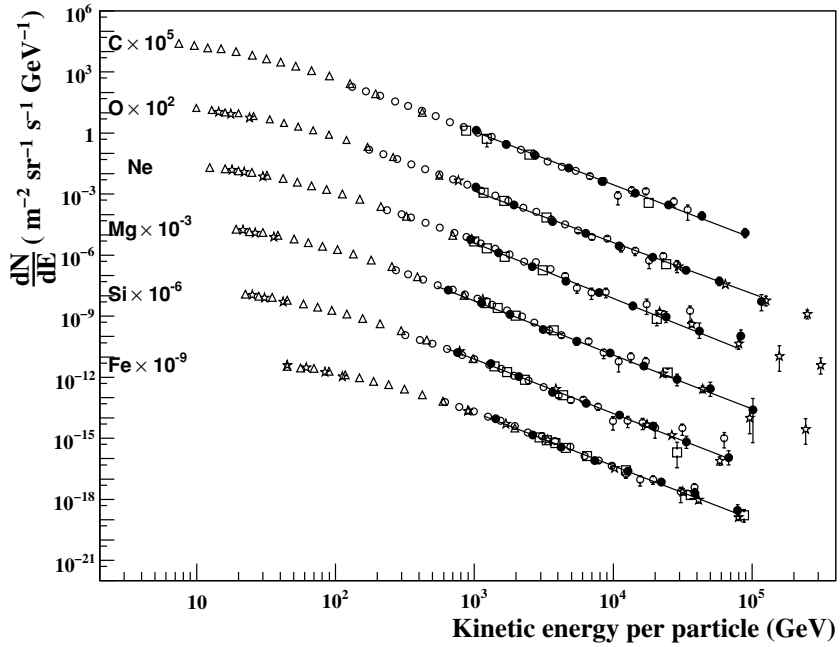

Figure 6. Differential intensity as a function of the kinetic energy per particle for cosmic-ray nuclei C, O, Ne, Mg, Si and Fe, respectively. CREAM-II data points (filled circles) are compared with previous observations from: *HEAO 3*–C2 (Engelman et al. 1990), triangles; CRN (Müller et al. 1991), squares; ATIC-2 (Panov et al. 2006), open circles; TRACER (Ave et al. 2008), stars. The solid line represents a power-law fit to the CREAM-II data. The fitted values of the spectral indices are listed in Table 2.

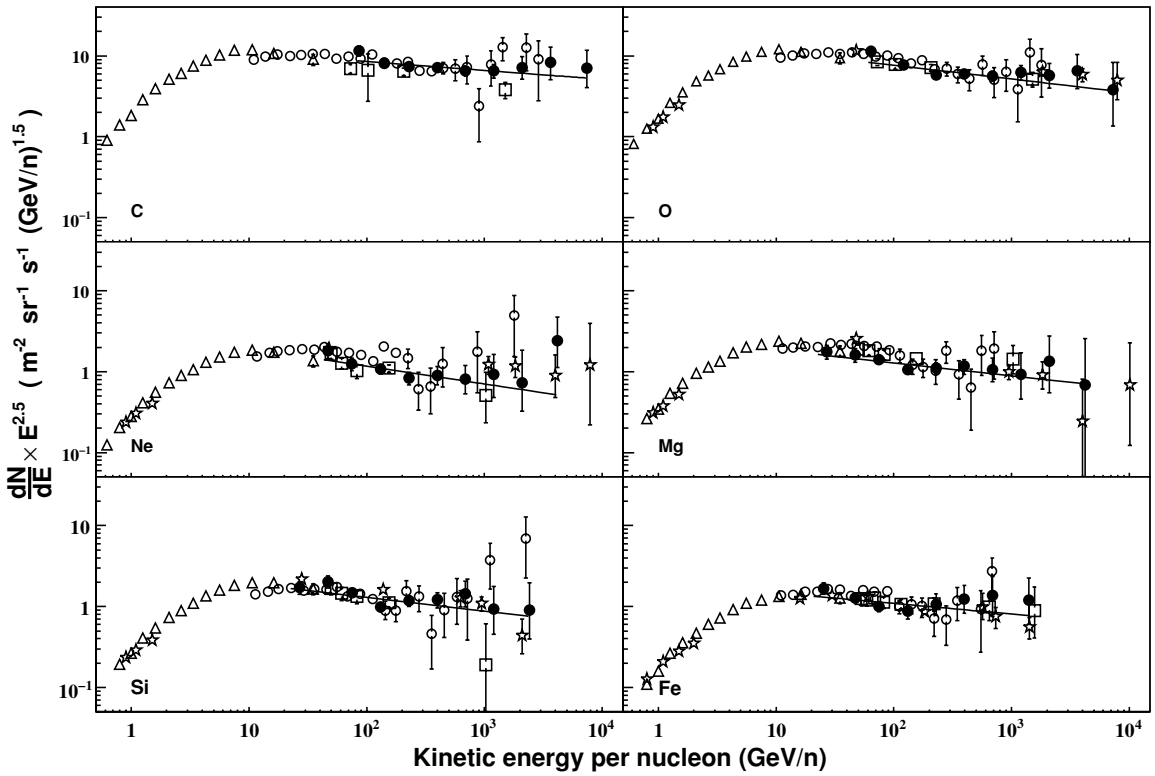

Figure 7. Energy spectra (per nucleon) for the elements C, O, Ne, Mg, Si, and Fe, respectively. The differential intensities are multiplied by $E^{2.5}$. CREAM-II results (filled circles) are compared with previous observations by: *HEAO 3*–C2 (Engelman et al. 1990), triangles; CRN (Müller et al. 1991), squares; ATIC-2 (Panov et al. 2006), open circles; TRACER (Ave et al. 2008), stars. The solid line represents a power-law fit to the CREAM-II data.

6. DISCUSSION

The CREAM-II results for primary nuclei are found to be in good agreement with previous measurements of space-based (*HEAO 3*–C2 (Engelman et al. 1990), CRN (Müller et al. 1991)) and balloon-borne (ATIC-2 (Panov et al. 2006), TRACER (Ave et al. 2008)) experiments (see Figures 6 and 7). All the elements appear to have the same spectral shape, which can be described by a single power law in energy $E^{-\gamma}$. The spectral indices fitted to our data (Table 2) are very similar, indicating that the intensities of the more abundant (evenly) charged heavy elements have nearly the same energy dependence. Our

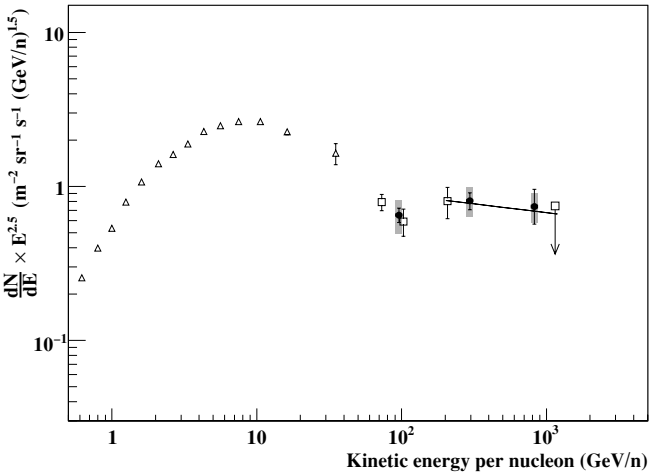

Figure 8. Measurements of the nitrogen energy spectrum (multiplied by $E^{2.5}$). CREAM-II results (filled circles) are compared with previous observations by *HEAO 3*–C2 (Engelman et al. 1990; triangles) and CRN (Swordy et al. 1990; squares). The error bars in CREAM-II data represent only the statistical errors, while the gray bands show the systematic uncertainties in the differential intensity. The solid line represents a power-law fit to the combined data at energies > 200 GeV/n. The fitted spectral index is 2.61 ± 0.10 (χ^2/ndf = 0.4/2).

observations, based on a calorimetric measurement of the CR energy, confirm the results recently reported by the TRACER collaboration (Figure 10), using completely different techniques (Cherenkov, specific ionization in gases and transition radiation) to determine the particle energy. The weighted average of our fitted spectral indices is $\bar{\gamma} = 2.66 \pm 0.04$, consistent, within error, with the value of 2.65 ± 0.05 obtained from a fit to the combined CRN and TRACER data (Ave et al. 2008). The great similarity of the spectral indices suggests that the same mechanism is responsible for the source acceleration of these primary heavy nuclei.

Although all the elemental spectra can be fitted to a single power law in energy, hardening (flattening) of the spectra above ~200 GeV/n is apparent from the overall trend of the data (Figure 7). A detailed analysis to investigate possible features in the spectra is in progress to evaluate the significance of a change in the spectral index.

CREAM-II data extend the energy range spanned by the previous elemental abundance measurements up to ~1 TeV/n (Figure 9). The C/O ratio measured by CREAM-II is consistent with the one reported by CREAM-I (Ahn et al. 2008) within the overlapping energy region covered by the two flights and slightly higher than the CRN result. The Ne/O and Mg/O ratios

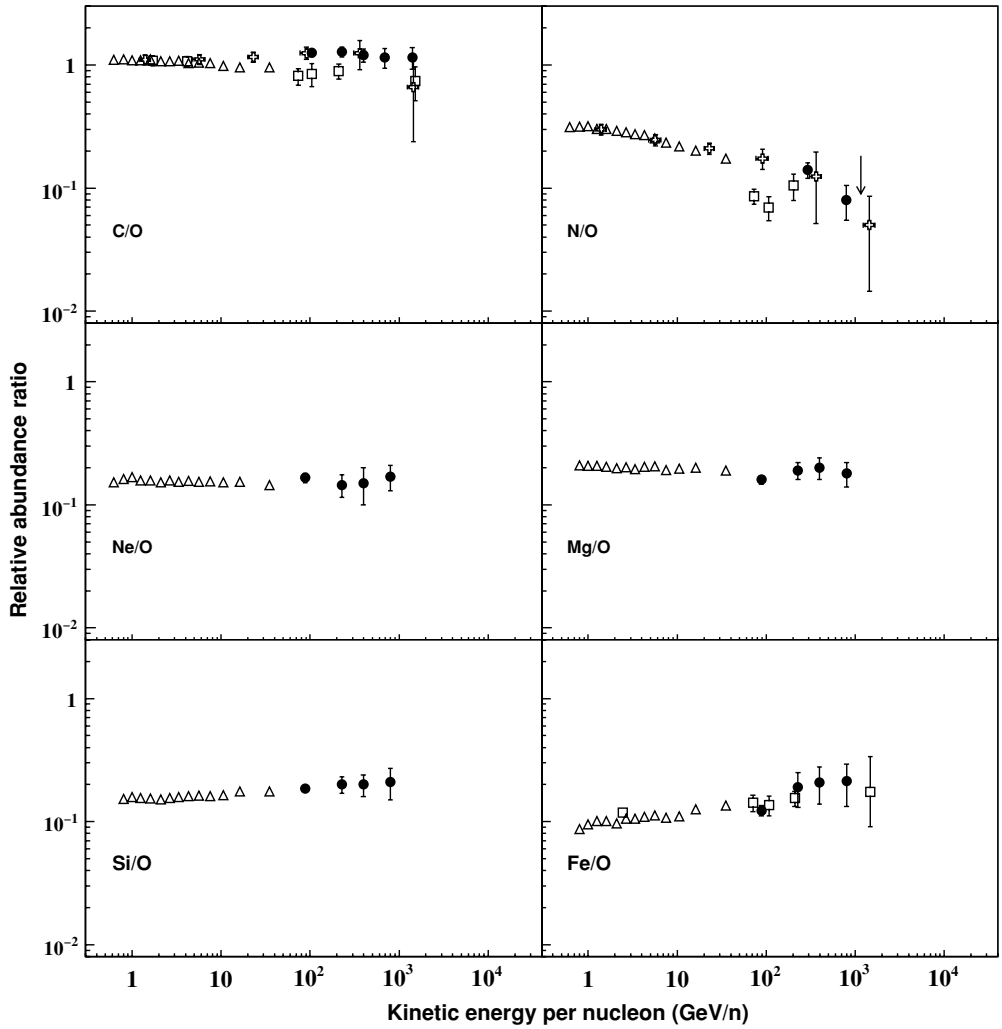

Figure 9. Measurements of the relative abundance ratios of C, N, Ne, Mg, Si, and Fe, respectively, to O as a function of energy. CREAM data from the first (open crosses) and second (filled circles) flight are compared with previous observations by *HEAO 3*–C2 (Engelman et al. 1990; triangles) and CRN (Swordy et al. 1990; squares). The arrow in the N/O plot is an upper limit set by CRN at 1.1 TeV/n.

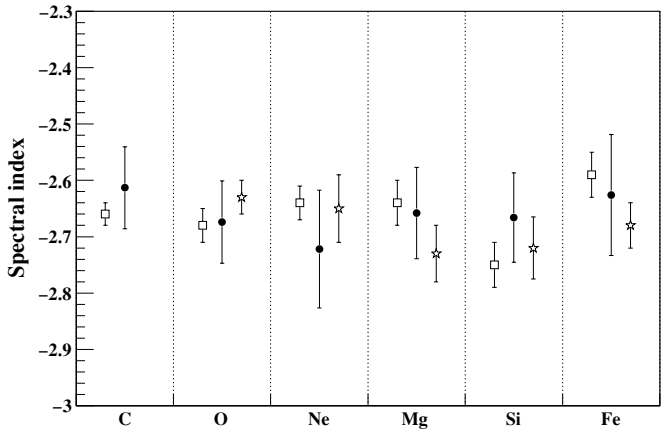

Figure 10. Fitted spectral indices (Table 2) from CREAM-II data (filled circles) are compared with the spectral indices of a power-law fit to: (stars) the combined CRN and TRACER data above 20 GeV/n (Ave et al. 2008); (open squares) a compilation of direct and indirect measurements (Wiebel-Sooth et al. 1998).

Table 2
Best-fit Values of the Spectral Index γ of Each Element, as Measured by CREAM-II, and χ^2/ndf of the Fit

Element	γ	χ^2/ndf
C	2.61 ± 0.07	3.3/7
O	2.67 ± 0.07	4.8/7
Ne	2.72 ± 0.10	4.2/7
Mg	2.66 ± 0.08	1.9/8
Si	2.67 ± 0.08	4.9/7
Fe	2.63 ± 0.11	4.2/6

confirm, up to 800 GeV/n, the nearly flat trend of *HEAO 3*–C2 low-energy data, while the fractions of Si and Fe with respect to O seem to increase with energy. This could represent the clue of a possible change in composition of CRs at high energies with an enhancement of heavier elements, as expected from SNR shock diffusive acceleration theories. Nevertheless, the statistics of the data are too limited for a definitive conclusion at this time.

Unlike the primary heavy nuclei, nitrogen is mostly produced by spallation in the interstellar medium, but it also has a primary contribution of order 10%, as recently measured by CREAM-I (Ahn et al. 2008). The measurement of nitrogen intensity at high energy is challenging because it requires an excellent charge separation between N nuclei and the much more abundant C and O neighbors, as well as a complete understanding of the corrections for secondary N particle production in the atmosphere and the instrument. The nitrogen data collected by CREAM-II are more statistically significant at high energy than any previous observation. We notice that, above 100 GeV/n, the N spectrum flattens out from the steep decline which characterizes the energy range 10–100 GeV/n (Figure 8). The combined CRN and CREAM-II data at energies higher than 200 GeV/n, are well fitted to a power-law in energy with spectral index 2.61 ± 0.10, consistent within the error with the average value $\bar{\gamma}$ of the primary nuclei. This supports the hypothesis of the presence of two components in the cosmic nitrogen flux. In fact, since the escape path length decreases rapidly with energy, the secondary nitrogen component is expected to become negligible at high energy, where only the primary component should survive. This might result in a change of the spectral slope, as observed.

As a cross-check to the measurement reported here, we calculate the relative abundance ratio of N/O and compare it with the CREAM-I observation (Figure 9), in which the energy of CRs was measured with a transition radiation detector. A N/O ratio (at the TOA) equal to 0.080 ± 0.025 (stat.) ± 0.025 (sys.) is measured at an energy of $\sim$800 GeV/n, in good agreement with recent results from CREAM-I (Ahn et al. 2008).

7. CONCLUSIONS

CREAM-II carried out measurements of high-Z CR nuclei with an excellent charge resolution and a reliable energy determination. The use of a dual layer of silicon sensors allowed us to unambiguously identify each individual element up to iron and to reduce the background of misidentified nuclei. We demonstrated the feasibility of measuring the particle energy up to hundreds of TeV by using a thin ionization sampling calorimeter, with sufficient resolution to reconstruct accurately the CR spectra.

The energy spectra of the major primary heavy nuclei from C to Fe were measured up to $\sim 10^{14}$ eV and found to agree well with earlier direct measurements. All the spectra follow a power law in energy with a remarkably similar spectral index $\bar{\gamma} = -2.66 \pm 0.04$, as is plausible if they have the same origin and share the same acceleration and propagation processes.

A new measurement of the nitrogen intensity in an energy region so far experimentally unexplored indicates a harder spectrum than at lower energies, supporting the idea that nitrogen has secondary as well as primary contributions. These results provide new clues for understanding the CR acceleration and propagation mechanisms, but further accurate observations with high statistics beyond 10^{14} eV are needed to finally unravel the mystery of CR origin.

This work is supported by NASA research grants to the University of Maryland, Penn State University, and Ohio State University, by the Creative Research Initiatives program (RCMST) of MEST/NRF in Korea, and INFN and PNRA in Italy. The authors greatly appreciated the support of NASA/WFF and NASA/GSFC, Columbia Scientific Balloon Facility, National Science Foundation's Office of Polar Programs and Raytheon Polar Services Company for the successful balloon launch, flight operation and payload recovery in Antarctica.

REFERENCES

Aharonian, F., et al. 2004, Nature, 432, 75
Ahn, H. S., et al. 2004, in Proc. 11th International Conference on Calorimetry in Particle Physics (Perugia, Italy), ed. C. Cecchi et al. (Singapore: World Scientific), 532
Ahn, H. S., et al. 2006, Nucl. Phys. B (Proc. Suppl.), 150, 272
Ahn, H. S., et al. 2008, Astropart. Phys., 30, 133
Ahn, H. S., et al. 2009, Nucl. Instrum. Methods A, 602, 525
Ave, M., et al. 2008, ApJ, 678, 262
Bell, A. R. 1978, MNRAS, 182, 443
Berezhko, E. G. 1996, Astropart. Phys., 5, 367
Binns, W. R., et al. 1988, ApJ, 324, 1106
Engelmann, J. J., et al. 1990, A&A, 233, 96
Fassò, A., Ferrari, A., Ranft, J., & Sala, P. R. 2005, FLUKA: A Multi-Particle Transport Code (CERN-2005-10 (2005), INFN/TC_05/11, SLAC-R-773; Menlo Park, CA: SLAC Nat. Accelerator Lab.), http://www.slac.stanford.edu/pubs/slacreports/slac-r-773.html
Gehrels, N. 1986, ApJ, 303, 336
Hillas, A. M. 2005, J. Phys. G: Nucl. Part. Phys., 31, R95
Hörandel, J. R. 2003, Astropart. Phys., 19, 193
Hörandel, J. R. 2004, Astropart. Phys., 21, 241
Kox, S., et al. 1987, Phys. Rev. C, 35, 1678
Lafferty, G. D., & Wyatt, T. T. 1995, Nucl. Instrum. Methods A, 355, 541

Lagage, P. O., & Cesarsky, C. J. 1983, A&A, 125, 249
Longair, M. S. 1994, High Energy Astrophysics 2 (Cambridge: Cambridge Univ. Press)
Marrocchesi, P. S., et al. 2004, Nucl. Instrum. Methods A, 535, 143
Marrocchesi, P. S., et al. 2008, Adv. Space Res., 41, 2002
Müller, D., et al. 1991, ApJ, 374, 356
Nam, S., et al. 2007, IEEE Trans. Nucl. Sci., 54, 1743
Nilsen, B. S., et al. 1995, Phys. Rev. C, 52, 3277
Panov, A. D., et al. 2006, Adv. Space Res., 37, 1944
Parizot, E., Marcowith, A., van der Swaluw, E., Bykov, A. M., & Tatischeff, V. 2004, A&A, 424, 747
Park, I. H., et al. 2007, Nucl. Instrum. Methods Phys. Res. A, 570, 286
Seo, E. S., et al. 2004, Adv. Space Res., 33, 1777
Sivher, L., et al. 1993, Phys. Rev. C, 47(3), 1225
Swordy, S. P., et al. 1990, ApJ, 349, 625
Tsao, C. H., et al. 1993, Phys. Rev. C, 47(3), 1257
Wiebel-Sooth, B., et al. 1998, A&A, 330, 389
Yanasak, N. E., et al. 2001, ApJ, 563, 768
Zei, R., et al. 2008, in Proc. 30th ICRC (Mexico City), 2, 23